Vibrational properties of LiNbO₃ and LiTaO₃ under uniaxial stress

Ekta Singh [1,*,†] Mike N. Pionteck [2,*,‡] Sven Reitzig [1] Michael Lange,[1] Michael Rüsing [1]
Lukas M. Eng [1,3] and Simone Sanna [2]

[1]*Institut für Angewandte Physik, Technische Universität Dresden, 01062 Dresden, Germany*
[2]*Institut für Theoretische Physik, Center for Materials Research (LaMa), Justus-Liebig-Universität Gießen, 35392 Gießen, Germany*
[3]*ct.qmat: Dresden-Würzburg Cluster of Excellence-EXC 2147, TU Dresden, 01062 Dresden, Germany*

Structural strain severely impacts material properties, such as the linear and nonlinear optical response. Moreover, strain plays a key role, e.g., in the physics of ferroelectrics and, in particular, of their domain walls. µ-Raman spectroscopy is a well-suited technique for the investigation of such strain effects as it allows to measure the lattice dynamics locally. However, quantifying and reconstructing strain fields from Raman maps requires knowledge on the strain dependence of phonon frequencies. In this paper, we have analyzed both theoretically and experimentally the phonon frequencies in the widely used ferroelectrics lithium niobate and lithium tantalate as a function of uniaxial strain via density functional theory and µ-Raman spectroscopy. Overall, we find a good agreement between our *ab initio* models and the experimental data performed with a stress cell. The majority of phonons show an increase in frequency under compressive strain, whereas the opposite is observed for tensile strains. Moreover, for E-type phonons, we observe the lifting of degeneracy already at moderate strain fields (i.e., at $\pm 0.2\%$) along the x and y directions. This paper, hence, allows for the systematic analysis of three-dimensional strains in modern-type bulk and thin-film devices assembled from lithium niobate and tantalate.

I. INTRODUCTION

Lithium niobate (LN) and lithium tantalate (LT) are cornerstone materials in nonlinear optics and optoelectronics with established applications ranging from second-harmonic generation [1,2], over optical ring resonators to holographic memory devices [3], to name just a few. These devices are based on bulk single-crystal platforms and have been constantly optimized over the past decades via meticulous analyses of crystal compositional aspects [4–6], degradation effects [7], defect distribution, and the precise imaging of domain structures [8–10]. Single-crystalline LN (or LT) thin films on insulating substrates have recently opened up a completely new scenario. This new platform allows for much higher integrability into existing nanoelectronic and nanophotonic structures [11,12] and outperforms bulk-based devices due to the submicron-scale confinement of optical modes [13–15].

Nevertheless, the transition towards thin-film LN devices emphasizes the importance of crystal properties that so far have played a minor role in LN bulk investigations and device fabrication. Among these, we count the increased influence of mechanical stress (σ) fields [16,17], e.g., due to the bonding process of the LN thin film onto the substrate, or occurring as a result of the poling procedure or waveguide fabrication, which

is paramount for the reliable and reproducible production of highly efficient nonlinear optical devices. Accumulated stress does not only increase the chance of critical failure (e.g., due to delamination) [16,17], but also influences optical key properties, such as refractive indices [18,19], and, thus, endangers the optical responses of a periodically poled domain grid [20].

Among established imaging techniques applied for the analysis of LN platforms, Raman spectroscopy can provide critical information about internal mechanical stress. To discriminate the influence of stress fields from other factors, e.g., electrical fields [21] or compositional heterogeneity [22], and to quantify occurring stress markers, it is essential to gain fundamental knowledge on the relation of phonon properties and mechanical stress fields. To date, the only investigations in this regard were conducted via hydrostatic pressure cells [23,24]. However, such experiments only investigate the influence of isotropically applied stress. In reality, effects, such as stress fields in the vicinity of LN domain walls (DWs), or mechanical stress in LN thin films, are not isotropic [25,26]. Under these environments, the directionality of stress largely changes the materials properties. Therefore, it is necessary to theoretically predict and experimentally verify the influence of uniaxial stress on phonon properties. This then provides a fundamental reference for future investigations of mechanical stress fields, in analogy to the reference work of Stone *et al.* [21] for incident electrical fields.

In this paper, we first provide the theoretical prediction on the evolution of the phonon properties in LN and LT crystals upon uniaxial compression along all three crystal axes via density functional theory (DFT) in Sec. II A. Second, we

---

*These authors contributed equally to this work.
†ekta.singh1@tu-dresden.de
‡mike.pionteck@theo.physik.uni-giessen.de

combine a piezodriven uniaxial stress cell with a μ-Raman spectroscopy setup to enable the experimental study of stress on the LN crystals. Experimentally, we compare stoichiometric and 5% MgO-doped LN samples compressed along the x, y, and z axes [see Sec. II B]. Section III C then provides a discussion of the calculated and measured data.

With this paper, we, thus, provide a basis for the quantitative, local stress analysis in LN and LT platforms via μ-Raman spectroscopy, and give a reference for the deeper understanding and further optimization of LN- and LT-based devices.

II. METHODOLOGY

A. Computational approach

The DFT calculations are performed within the generalized gradient approximation [27] in the formulation of Perdew, Burke, and Ernzerhof [28] as implemented in the Vienna *ab initio* simulation package [29]. Thereby, projector augmented wave [30] potentials with projectors up to $l = 3$ for Nb and Ta, and $l = 2$ for Li and O have been used, which proved to be accurate enough as demonstrated in a previous work [31]. The electronic wave functions are expanded into a plane-wave basis set up to kinetic energy of 475 eV. In order to model uniaxial stress, the lattice constants of the rhombohedral unit cell were adjusted according to the expression,

$$\boldsymbol{a}_n(\epsilon) = (\boldsymbol{I} + \epsilon)\boldsymbol{a}_n(0), \tag{1}$$

where ϵ, $\boldsymbol{I}$, $\boldsymbol{a}_n(0)$, and $\boldsymbol{a}_n(\epsilon)$ denote the strain tensor, the identity matrix, and the nth unstrained and strained lattice vector, respectively. The strain tensor was then calculated using the elastic compliance tensor S from Ref. [32],

$$\epsilon = S\sigma, \tag{2}$$

and the boundary conditions for uniaxial stress [33]. This means that all components of the stress tensor σ are set to zero, except for the component in the direction of which uniaxial stress is to be exerted. For instance, if uniaxial stress is to be calculated along the x direction, $\sigma_1 \neq 0 = \sigma_2 = \sigma_3 = \sigma_4$ (Voigt notation) is set as boundary condition. As a result, the strain tensor for uniaxial stress can be calculated using the elastic compliance tensor from Ref. [32] and Eq. (2). Subsequently, this strain tensor and Eq. (1) are used to calculate the strained lattice vectors under uniaxial stress. By calculating the strained lattice vectors using the compliance tensor, the Poisson ratio, and the shear strain are explicitly considered. Due to constraints of the unit-cell sizes, only stoichiometric LN and LT are calculated. However, as later demonstrated by experiments by comparing 5% MgO-doped and stoichiometric LN, it is shown that the results for 5% MgO-doped and stoichiometric LN are comparable, therefore, this assumption is justified to only calculate stoichiometric LN and LT.

The calculations were performed in two ranges for LN and LT: First, the effects of strain, i.e., compressive as well as tensile strain, on the phonon frequencies have been calculated in fine increments up to values reachable in the experiments. Second, calculations for higher values of strains but more coarse increments were performed. For LN and LT this procedure has been performed for lower strains up to 0.10%, as well as for higher values up to 2.4%. Here, increments of 0.02% and 0.4% have been chosen, respectively. The

Hellmann-Feynman forces are minimized under a threshold value of 0.005 eV/Å by relaxation of the atomic positions. In this procedure, all lattice vectors calculated from Eq. (1) are fixed. For our calculations of unstrained structures, we have used commonly accepted experimental lattice constants ($a_R^{LN} = 5.494$ Å, $\alpha^{LN} = 55.867°$, and $a_R^{LT} = 5.474$ Å, $\alpha^{LT} = 56.171°$) [31].

The Γ-centered phonon frequencies and eigenvectors are derived by the frozen-phonon method [34] without symmetry constraints. For the calculation of the Hessian matrix, atomic displacements of 0.015 Å in each Cartesian direction are considered. Since our approach does not take into account the long-range electric fields accompanying the longitudinal-optical (LO) phonons, our calculations are restricted to transversal-optical (TO) phonons, only. A $8 \times 8 \times 8$ k-point mesh is used to sample the first Brillouin zone corresponding to the orthorhombic unit cell, which yields 192 irreducible points.

B. Experimental procedure

In order to complement the above theoretical investigations, we measured the frequency shift of the phonon modes in LN by combining μ-Raman spectroscopy with a uniaxial stress cell [35]. All measurements were performed using a LabRAM HR spectroscope from Horiba in 180° backscattering geometry. In this setup, a HeNe laser at 632.8 nm wavelength was focused onto the samples using a 100× and 0.9 numerical-aperture objective. For each data point, two acquisitions were collected for 10 s each whereas using a diffraction grating of 1800 grid lines per millimeter for spectral analysis. For these settings, the corresponding spectral resolution is 0.56 cm^{-1}, which was determined as part of the calibration using a He-Ne gas discharge lamp. Here, the plasma line at a wavelength of 671.7 nm has a natural linewidth of 0.025 nm (0.56 cm^{-1}), which corresponds to the spectral resolution, i.e., the standard deviation, which only means how well the two overlapping peaks can be resolved. On the other hand, with the help of the standard error obtained from peak fitting, each peak center can be pinpointed with 100–1000 times more precision, and this is the quantity we are interested in.

All the samples used in this paper were firmly attached to the uniaxial stress cell using black stycast epoxy resin [36] such that the strain is fully transmitted to the sample through the epoxy resin. The force applied to the sample was directly measured through a force sensor attached to the back of the device. This force was later converted to stress using the relation,

$$\sigma = \frac{F}{A}, \tag{3}$$

where A denotes the cross section of the samples provided in Table I, and F is the force measured by the force sensor. In order to compensate for any charge-induced effects due to the piezoelectric effect, the top and bottom faces of the sample surfaces were electrically grounded using 10 nm-thick chromium electrodes. All the measurements were always performed across the chromium electrodes, which at the given thickness are still sufficiently transparent and do not affect our

TABLE I. Description of the samples used for the experimental stress measurement analysis.

Sample name	Description	Size	Stress axis
sLN-x	z-cut stoichiometric LN	$y \times z$: 580×113 μm^2	x
sLN-y	z-cut stoichiometric LN	$x \times z$: 580×113 μm^2	y
5 Mg-LN-x	z-cut 5%-MgO doped LN	$y \times z$: 500×140 μm^2	x
5 Mg-LN-y	z-cut 5%-MgO doped LN	$x \times z$: 400×100 μm^2	y
5 Mg-LN-z	x-cut 5%-MgO doped LN	$y \times$ x: 400×100 μm^2	z

measurements as also shown in the past for *in situ* second-harmonic microscopy studies [37].

A total of five samples were measured [see Table I]. First, stoichiometric LN, being close to the ideal crystals considered for the theoretical calculations, is measured and used to compare theory with experiment. Second, 5% MgO-doped LN samples are chosen because they are widely used among the ferroelectrics and integrated optics community due to their low photorefraction and highly conductive domain walls [12,38–40]. Comparing the results on the stoichiometric and MgO-doped crystals allows us to see whether or not there are any stoichiometry-specific changes in the responses, which would also not be covered by the DFT calculations.

1. Data extraction method

The Raman spectra of single-crystalline LN and LT are well understood and have been investigated thoroughly before [31,41–44]. The optical phonons of LN and LT consist of four A_1, five A_2, and nine doubly degenerated E phonon branches. Here, A_1 and E are optical branches and are both Raman and infrared active. In contrast, the A_2 branch is optically inactive. Furthermore, depending on the scattering geometry, these branches either appear as TO or LO modes. Conveniently LN and LT peaks are labeled by type of symmetry (A_1 or E), followed by the specific type (TO or LO) and consecutive number counting from low to high frequencies. For example, the phonon E(TO$_9$) labels the ninth, i.e., highest frequency, E-type TO phonon. The assignment of peaks in this paper has been performed according to the most recent accepted assignment by Margueron *et al.* [43], Sanna *et al.* [31], and Rüsing *et al.* [42].

Figures 1(a)–1(c) show example Raman spectra of the 5 Mg-LN-x, 5 Mg-LN-y, and 5 Mg-LN-z samples, respectively. These spectra are measured in different scattering geometries represented by the Porto notation $k_i(e_i, e_s)k_s$, where k_i and k_s represent the directions of the incident and scattered light in crystal coordinates, and e_i and e_s denote the directions of polarization of both incoming and Raman-scattered beams, respectively [42]. Here, each plot contains three spectra where spectrum A belongs to the unstressed (0 MPa) state of the sample whereas spectrum B describes a compressed state of the sample. The third is the difference spectrum of the former two. To eliminate the intensity influences in the difference spectrum and to solely highlight the effect of the frequency shift due to applied stress, all the spectra were first normalized individually by subtracting the noise background (if applicable) and divided by the intensity of the highest peak [10]. From the different spectra in Fig. 1(b), it can be clearly noted that the frequency of the E(TO$_1$) phonon mode in $\overline{Z}$(XY)Z

geometry increased under compression, whereas the frequency for A_1(TO$_1$) in $\overline{X}$(ZZ)X geometry decreased. Apart from these large differences, further changes are difficult to note. So, to quantify frequency shifts as a function of stress, the fitting of the spectra by Lorentzian functions is performed. In this way, the frequencies at the maxima of the phonon peaks were determined for different stress values and plotted against applied stress, such as shown in Fig. 2. Via statistical analysis of the phonon shifts, we are able to deduce the experimental phonon-stress-shift coefficients with a precision of 0.01 cm^{-1}/%.

Additionally, it is well known [45,46] that the spectra of congruent or MgO-doped LN show broader and less-resolvable peaks as compared to the stoichiometric LN. Here, various peaks overlap with each other that then leads to a more challenging peak assignment. For example, the pairs E(TO$_3$)-A_1(LO$_1$), A_1(LO$_2$)-E(TO$_4$), and A_1(LO$_3$)-E(TO$_7$) overlap with each other in the $\overline{Z}$(XX)Z and $\overline{Z}$(YY)Z geometry of MgO-doped LN. Therefore, in Sec. III A, to avoid any misleading conclusions for these peaks the Raman shifts with the stress have not been fitted [see Tables II and IV].

Furthermore, to find an optimum location on the sample, a series of optimization measurements [47] are performed. As a result, all the measurements were performed in the center of the sample and 10 μm below the sample surface.

III. RESULTS

A. Experimental results

For the sake of simplicity, we only show the pressure dependency for selected phonon modes; the complete results are shown in the Supplemental Material (SM) [47].

Figure 2 shows the response of the E(TO$_1$) phonon mode under x and y compression for both the stoichiometric and 5%-MgO doped LN samples. The three curves in a single plot represent the three different scattering geometries given in Porto's notation. Since the change in the frequency ($\Delta\omega$) with respect to the unstressed state is the quantity of interest, we have plotted the frequencies with respect to the 0 MPa value as a function of stress. Hence, we also account for any offset due to sample mounting or bending effects as discussed in the SM [47]. The colored region around the fitted lines show the one-σ confidence interval, calculated from linear fitting which included the standard error of individual peaks. The E(TO$_1$) mode shows a linear positive slope for the compression in all cases. In the case of x compression for both sLN-x and 5 Mg-LN-x samples, the slope is larger in $\overline{Z}$(YY)Z measurement geometry. On the other hand, when the same samples are compressed along the y crystallographic axis, the slope
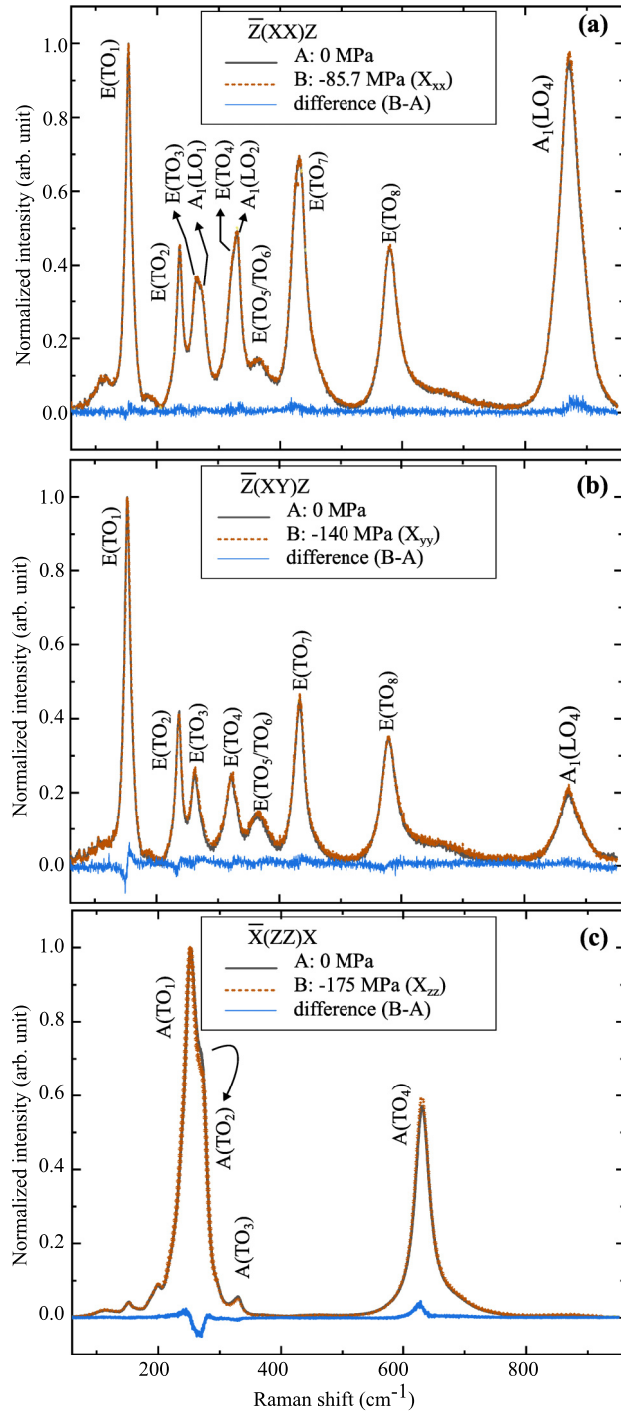
FIG. 1. (a) $\overline{Z}(XX)Z$ Raman spectra of unstressed (0 MPa) and *x* compressed (-85.7 MPa) 5% MgO-doped LN (5 Mg-LN-*x*). (b) $\overline{Z}(XY)Z$ Raman spectra of unstressed (0 MPa) and *y* compressed (-140.7 MPa) 5% MgO-doped LN (5 Mg-LN-*y*). (c) $\overline{X}(ZZ)X$ Raman spectra of unstressed (0 MPa) and *z* compressed (-175 MPa) *z* axis of 5% MgO-doped LN (5 Mg-LN-*z*). The difference curve in all (a)–(c) graphs represents the difference spectra between the stressed and unstressed states of the sample.

is larger for $\overline{Z}(XY)Z$ and $\overline{Z}(XX)Z$ scattering geometries. We have observed this behavior for almost all the phonon modes [47]. The value of different slopes in different measurement geometries can be interpreted as the lifting of the twofold

degeneracy of the E modes predicted by theory as discussed below.

When comparing 5 Mg-LN-*x*/-*y* and sLN-*x*/-*y*, the slopes are similar as shown in Fig. 2. The origin of the small deviations could be due to the presence of defects in doped LN. This argument is consistent with the work performed by Tejerina *et al.*, where they show that doping increases the phonon shift under hydrostatic pressure ($\Delta\omega/\Delta\sigma$) [48], especially for the $A_1(TO_2)$, $A_1(TO_3)$, and $E(TO_4)$ phonon modes. The comparison for other peaks is also summarized in Table II.

As will later be shown by theory, the phonon frequency should decrease under tension with a slightly different magnitude. That is why the phonon response of sample sLN-*x* is also measured experimentally in $\overline{Z}(YY)Z$ scattering geometry under tension. For tensile strain, the opposite response is observed as expected: the frequency decreased on applying tension to the sample. For example, phonon mode $E(TO_6)$ shows the largest response as for compression with a slope of -8.15 ± 2.88 cm^{-1}/GPa. The plot for $E(TO_6)$ and the slopes for all peaks are provided in the SM [47].

B. Strain simulation

First, to assess the quality of the models in this paper, the calculated phonon frequencies of unstrained stoichiometric LN and LT are compared with previous works [31,47] (all data appear in the SM). Compared to our experiment, the largest deviation from the experimental values for LN and LT occurs for the $A_1(TO_4)$ mode with 20 and 22 cm^{-1}, respectively. The mean deviation from experimental values for LN and LT is about 8.7 and 8.4 cm^{-1}. Thus, compared with the mean deviation of the theoretical results of Ref. [31] which was about 10.7 and 10.8 cm^{-1} for LN and LT, there is a close agreement with both the theoretical and the experimental values. In addition, the typical deviations are also consistent with literature values, such as Refs. [42,49].

In order to demonstrate the dependence of the phonon frequencies predicted by our calculations, the $E(TO_4)$ mode of LN was chosen [see Fig. 3]. Figures 3(a) and 3(b) show the results of the calculations with lower and higher strains, respectively. The frequency shift of the $E(TO_4)$ mode has an approximately linear dependence on the applied compression. Such a linear dependence is observed in all of our calculations for each mode for both the compressive and the tensile strain in stoichiometric LN and LT. This is consistent with the results of LN and LT under hydrostatic pressure by Mendes-Filho *et al.* [23]. In Fig. 3(a) the frequency increases up to 6 cm^{-1} and in (b) up to 0.3 cm^{-1}.

Our calculations predict for stoichiometric LN and LT that the degeneracy of the E modes is lifted under strain applied along the *x* and *y* directions due to the reduction of the threefold symmetry. This results in splitting into two branches, which is consistent with previous studies on various two-dimensional (2D) materials, that reported a mode splitting under strain due to the reduction of symmetry [50,51]. Consequently, for strains applied along the *x* and *y* directions, all E modes are considered separately. For example, the $E(TO_9)$ mode for compression in *x* and *y* directions has a significant splitting [see Fig. 4(a)]. In contrast, it is noticeable that the $E(TO_9)$ mode remains degenerate for *z* compression since the
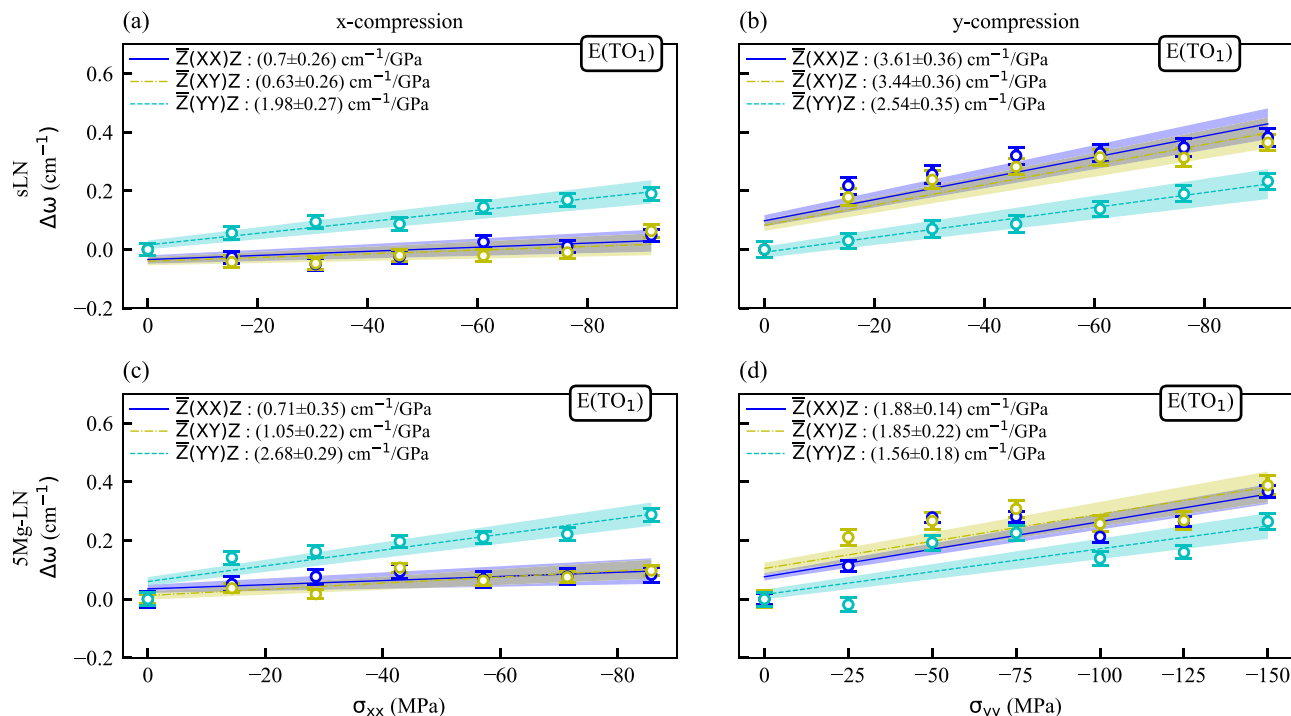
FIG. 2. Measured response of the $E(\text{TO}_1)$ phonon mode (a) and (b) in the samples sLN compressed along the x and y axes, respectively and (c) and (d) in the sample 5 Mg-LN compressed along the x and the y axes, respectively. The stoichiometric and 5% MgO-doped LN behave similarly.

considered strains in the z direction of both LN and LT do not lead to any reduced symmetry. This is the case for all E modes of LN and LT under strain.

Since the slopes, for strains in the x and y directions of LN and LT, are very similar [47] due to the symmetry of the crystals, Table III shows only the slopes for strain in the x direction. With the exception of the $A_1(\text{TO}_1)$ and $A_1(\text{TO}_4)$ modes, compressive strain leads to an increase in frequency, whereas tensile strain leads to a decrease in frequencies, which is consistent with results from previous research on other materials [52,53]. Comparing the slopes under the com-

pressive and tensile strain of LN, we find that they hardly differ for the individual modes. This behavior is not surprising, however, it is not universal as shown for a 2D material by Pak *et al.* [52]. Although under both compressive and tensile strains the $E(\text{TO}_{5/6})$ modes have the largest frequency shifts, the $E(\text{TO}_6)$ mode has a larger slope than the $E(\text{TO}_5)$ mode under compression. However, this relation turns around under tensile strain as can be seen in Table III. This applies to strain in the x and y directions for both LN and LT [47].

In addition, the results of LT under compression are listed in Table III for the same modes. In direct comparison with the

TABLE II. Experimentally determined Raman shift changes $\Delta\omega$ as a function of stress σ for x compression. The slopes were obtained after linearly fitting the experimental changes in frequency upon x compression. An asterisk labels silent modes [42]. In the case of 5% MgO-doped LN, many peaks overlap with each other [see Figs. 1(a) and 1(b)], therefore, extracting the peak frequency with an acceptable error was not possible. This is represented by the "−" sign.

| Phonon modes	sLN-x (cm^{-1}/GPa)			5 Mg-LN-x (cm^{-1}/GPa)		
	$\overline{Z}(XX)Z$	$\overline{Z}(XY)Z$	$\overline{Z}(YY)Z$	$\overline{Z}(XX)Z$	$\overline{Z}(XY)Z$	$\overline{Z}(YY)Z$
$A_1(\text{LO}_1)$	2.13 ± 0.52	*	2.06 ± 0.58		*	
$A_1(\text{LO}_2)$	3.29 ± 0.17	*	3.66 ± 0.17		*	
$A_1(\text{LO}_3)$	0.39 ± 0.94	*	0.29 ± 0.71		*	
$A_1(\text{LO}_4)$	1.96 ± 0.21	*	2.32 ± 0.19	3.07 ± 0.83	*	3.79 ± 0.80
$E(\text{TO}_1)$	0.70 ± 0.26	0.63 ± 0.26	1.98 ± 0.27	0.71 ± 0.35	1.05 ± 0.22	2.68 ± 0.29
$E(\text{TO}_2)$	0.34 ± 0.17	0.26 ± 0.25	1.68 ± 0.16	-0.51 ± 0.45	-0.63 ± 0.52	1.52 ± 0.3
$E(\text{TO}_3)$	1.28 ± 0.44	1.39 ± 0.65	1.67 ± 0.42			
$E(\text{TO}_4)$	2.12 ± 0.35	1.56 ± 0.59	3.02 ± 0.4			
$E(\text{TO}_{5/6})$	6.36 ± 0.98	6.25 ± 1.5	8.17 ± 0.87	5.87 ± 4.23	3.77 ± 3.69	9.38 ± 2.16
$E(\text{TO}_7)$	0.44 ± 0.37	0.86 ± 1.51	1.24 ± 0.22			
$E(\text{TO}_8)$	-0.47 ± 0.30	0.37 ± 0.36	3.03 ± 0.27	-0.29 ± 0.8	1.66 ± 0.69	4.32 ± 0.67
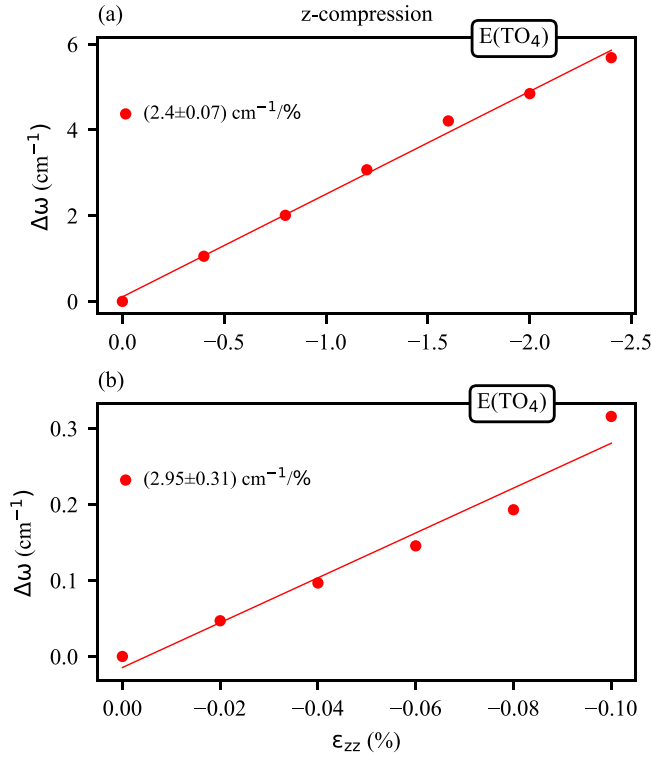
FIG. 3. DFT calculated relative frequency shifts of the $E(TO_4)$ mode of stoichiometric LN as a function of strain in z direction in (a) steps of 0.4 % and (b) steps of 0.02 %. The linear fit and the standard deviation of both are plotted and their parameters displayed. The slopes for strain are defined as $(\Delta\omega)/(|\Delta\epsilon|)$ and displayed with the fitting error.

results of LN, they are very similar along both directions as well as magnitude. This is in agreement with Mendes-Filho *et al.* [23] and expected since LN and LT are isostructural. Nevertheless, there are some small deviations. In particular, the degeneracy lifting is attenuated compared to LN. For

TABLE III. Calculated slopes of transversal A_1 and E modes of stoichiometric LN under compressive and tensile strain, and stoichiometric LT under compressive strain in the x-direction at higher strains in cm^{-1}/%. The slopes for strain are defined as $(\Delta\omega)/(|\Delta\epsilon|)$.

Phonon mode	LN comp. $\Delta\omega$ (cm^{-1}/%)	LN tens. $\Delta\omega$ (cm^{-1}/%)	LT comp. $\Delta\omega$ (cm^{-1}/%)
$A_1(TO_1)$	0.22	−4.49	3.46
$A_1(TO_2)$	4.45	−3.03	5.08
$A_1(TO_3)$	4.82	−7.18	4.69
$A_1(TO_4)$	6.35	−1.03	3.74
$E(TO_1)$	0.48/4.24	−0.61/−2.81	2.25/1.03
$E(TO_2)$	1.74/−0.14	−2.11/−0.11	0.46/3.59
$E(TO_3)$	1.48/3.27	−3.67/−1.05	3.05/2.82
$E(TO_4)$	4.28/−0.11	−4.49/−0.12	2.58/2.90
$E(TO_5)$	6.20/6.94	−8.90/−13.24	10.76/8.61
$E(TO_6)$	12.80/11.03	−7.62/−4.45	13.64/14.27
$E(TO_7)$	4.18/2.40	0.11/0.15	2.00/1.42
$E(TO_8)$	2.87/−0.55	−7.08/0.70	5.30/3.25
$E(TO_9)$	−0.67/7.06	2.98/−7.02	4.77/4.79

instance, the upper branch of the $E(TO_1)$ mode has a notable lower slope than that of LN. Also, the $E(TO_9)$ mode exhibits a significantly attenuated degeneracy lift for LT under compression than for LN. These deviations can be explained with the help of the eigenvectors. In Fig. 5 the eigenvectors of $A_1(TO_{1-4})$ and $E(TO_{1-9})$ are shown in the rhombohedral unit cell [31,42]. Such modes with high vibrational contributions from Nb and Ta ions, such as the $E(TO_1)$ mode, lead to a slightly different vibrational behavior [31]. The modes that have, in turn, low contributions of Nb and Ta ions with respect to their eigenvectors are very similar under compression of LN and LT. Since in the $E(TO_9)$ mode, the displacement of O is more involved than that of Nb/Ta, the reason for the difference between LN and LT may be due to the nature of Nb/Ta-O bond, similar to observations in Refs. [31,42]. The mean Nb-O distance (2.02 Å) is larger than that of Ta-O (2.00 Å). Stronger bonding with the oxygen atoms, and, thus, larger deformation of the oxygen octahedron, might be the reason for the difference between LN and LT concerning the $E(TO_9)$ mode. Also, slight differences in $E(TO_7)$ and $E(TO_8)$, which are pure distortions of the oxygen octahedron, might be related to the different Nb/Ta-O bonds.

The $E(TO_{5/6})$ and $A_1(TO_2)$ modes are characteristic for LN and LT under strain since these have particularly high slopes as shown in Table III and Figs. 4(b) and 4(c). This is also in agreement with Ref. [23]. The $E(TO_{5/6})$ are especially sensitive to strain in the x and y directions. This can be explained by a simple analysis of their eigenvectors. In Fig. 5 it can be seen that these two modes, in contrast to all other modes, are characterized by particularly large displacements of the lithium ions parallel to the x-y plane. Hence, these modes are most affected when the distances between the ions parallel to the x-y plane are shortened. The $A_1(TO_2)$ mode has among the largest slope for strain along the z direction. This can be reasonably explained in terms of the eigenvectors as well. As seen in Fig. 5, the ions of the $A_1(TO_2)$ mode vibrate in the z direction. When compression in the z direction shortens the bond length between the ions parallel to their displacement, the frequency is expected to increase. As the eigenvectors of the $A_1(TO_2)$ mode point most in the z direction, it, consequently, has the largest slope compared to all other modes when compressed in the z direction. All further data and results on LN and LT under compressive and tensile strain are provided in the SM [47].

C. Discussion: Comparing theory and experiment

As mentioned in the Introduction section, the calculations are performed in units of strain, and the experiments are performed in units of stress. In order to compare both results we have converted the experimental values of stress into values of strain using the equation given below,

$$\sigma = E\epsilon, \tag{4}$$

where E is Young's modulus of a sample [54]. The calculated value of Young's moduli of LN along the x, y, and z axes are 173.6, 173.07, and 201.0 GPa, respectively [47]. For every measured stress, we calculated the respective strain value and plotted the corresponding frequency shift along with the theoretical data as a function of strain [see Fig. 6]. Since the
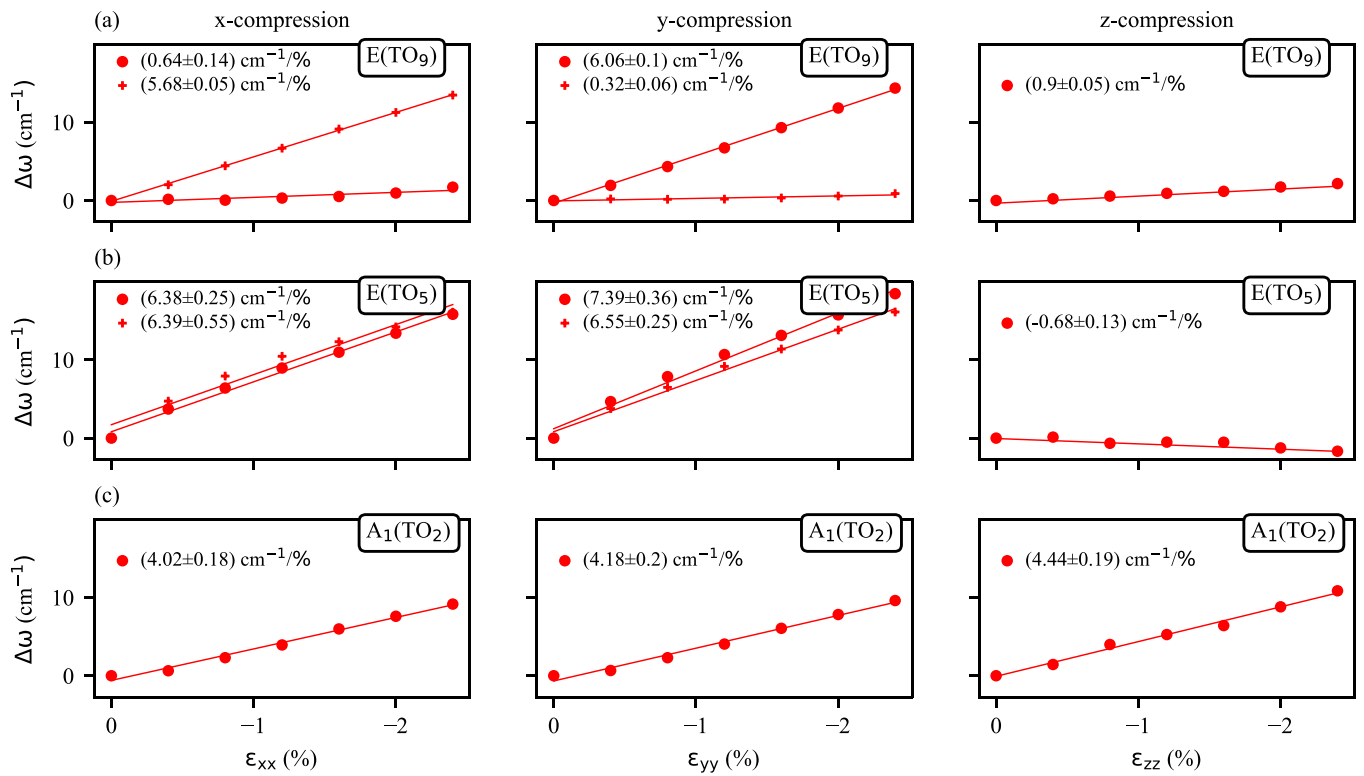
FIG. 4. The DFT calculated relative frequency shifts of (a) $E(TO_9)$ (first row), (b) $E(TO_5)$ (second row), and (c) $A_1(TO_2)$ (third row) modes of stoichiometric LN as a function of strain in steps of 0.4 % along the x, y, and z directions. The slopes for strain are defined as $(\Delta\omega)/(|\Delta\epsilon|)$ and displayed with the fitting error.
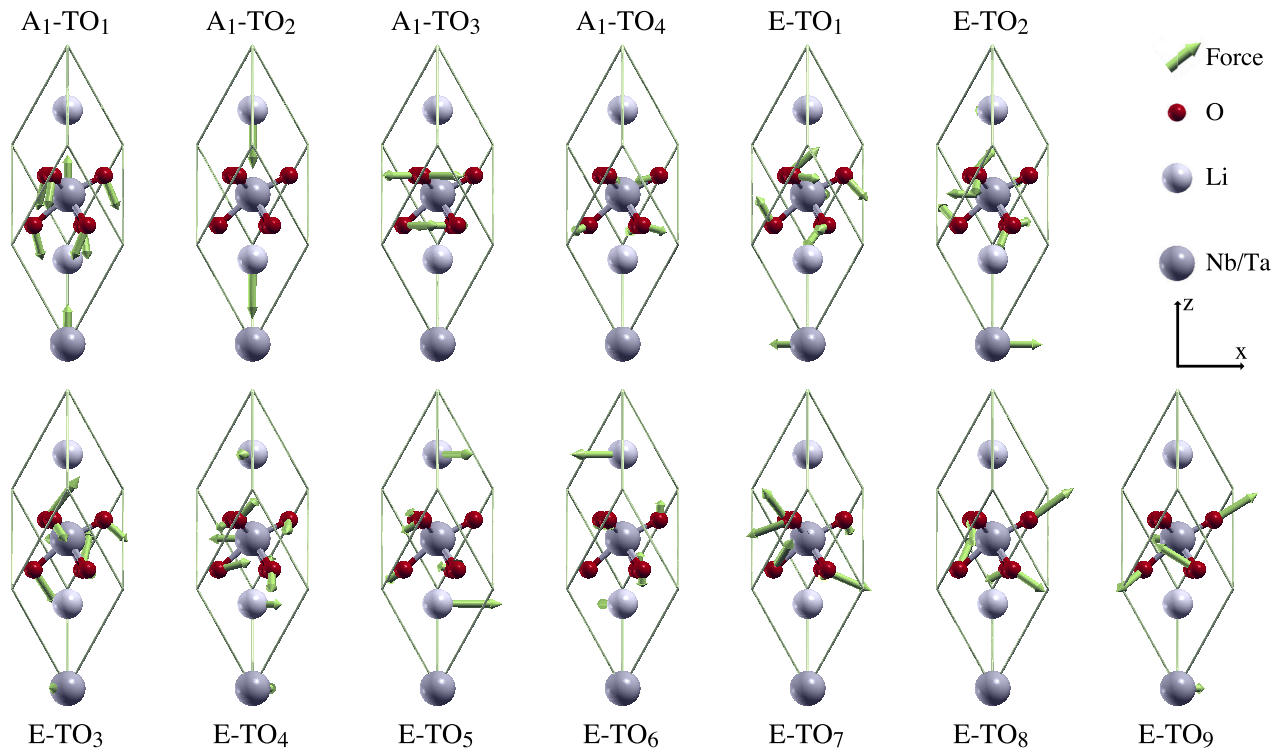

FIG. 5. The eigenvectors of the Raman-active vibrations of unstrained stoichiometric LN and LT in the rhombohedral unit cell of the transversal phonon modes with A_1 and E symmetries. Thereby light gray is denoted as Li, dark gray is denoted as Nb/Ta, and red is denoted as an O ion, whereas the green arrows represent the displacement direction.
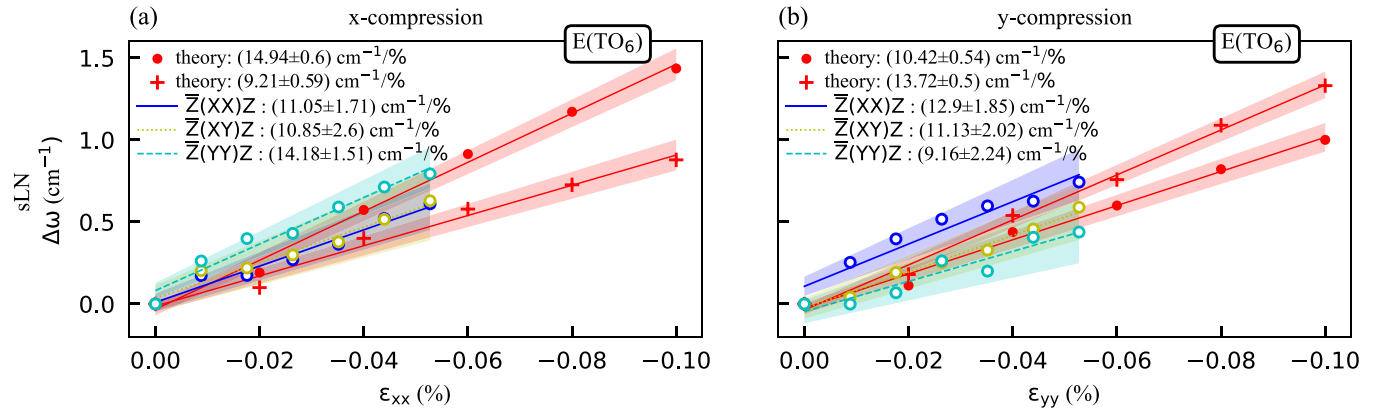
FIG. 6. Comparison of the experimental and theoretical frequency shifts (at lower strains): (a) and (b) $E(TO_6)$ phonon mode under compression along the x and y axes of stoichiometric LN. The shaded region around all the curves is the confidence interval of the linear fit.

stoichiometric samples are the closest system to the stoichiometric system considered for theoretical calculations, they are compared with theoretical data in Fig. 6.

For x compression, theoretically, the $E(TO_6)$ mode shows lifting of the degeneracy in accordance with the results of Sec. III B. For a more accurate comparison, the slopes for higher strains for y and z compression are listed in Table IV. The theoretical results on the degeneracy lifting offer a new interpretation of the experimental results. In particular, comparing the data for the $E(TO_6)$ mode with compression in the x direction, it can be seen that the measured data for the $\overline{Z}(YY)Z$ resembles the calculated upper branch, whereas the measured data for the $\overline{Z}(XY)Z$ and $\overline{Z}(XX)Z$ geometry is similar to the calculated lower branch. For y compression, the same can be observed with the $\overline{Z}(XY)Z$ and $\overline{Z}(XX)Z$ geometries having the higher slope, respectively, and the $\overline{Z}(YY)Z$ having the lower slope, i.e., the slopes flip for the y compression. Con-

sequently, it can be assumed that with the help of different scattering geometries the lifting of the degeneracy by x and y compressions can be reproduced experimentally.

Based on this interpretation, it can be concluded that the experimental and theoretical data fit very well. For a more accurate comparison, the slopes for higher strains for y and z compressions are listed in Table IV.

Interpreting the experimental data as lifting the degenerate E modes on x and y compressions can also help characterize compressed LN. From the data, it can be implied that one has x compressed LN when the $\overline{Z}(YY)Z$ geometry measures a higher slope than for the $\overline{Z}(XY)Z$ and $\overline{Z}(XX)Z$ geometries. If, on the other hand, one has y compressed LN, this argument just reverts. In contrast, if no splitting of E modes is observed in different scattering geometries, it can be concluded that the LN under investigation must be a z-compressed sample. Furthermore, the experimental comparison in Fig. 6 and Table IV,

TABLE IV. Comparison between the theoretical response at higher strains with the experimental response of the samples sLN-y and 5 Mg-LN-z. Asterisks label modes that are Raman silent in the given scattering geometry.

| Modes	sLN-y (cm^{-1}/%)				5 Mg-LN-z (cm^{-1}/%)			
	$\overline{Z}(XX)Z$	$\overline{Z}(XY)Z$	$\overline{Z}(YY)Z$	Theory	$\overline{X}(ZZ)X$	$\overline{X}(YZ)X$	$\overline{X}(YY)X$	Theory
$A_1(LO_1)$	8.01 ± 1.41	*	6.31 ± 0.68	*	*	*	*	*
$A_1(LO_2)$	7.95 ± 0.35	*	6.18 ± 0.68	*	*	*	*	*
$A_1(LO_3)$	4.24 ± 1.94	*	2.82 ± 0.68	*	*	*	*	*
$A_1(LO_4)$	6.75 ± 0.33	*	5.12 ± 0.68	*	*	*	*	*
$A_1(TO_1)$	*	*	*	-0.09	-4.97 ± 0.93	*	-5.10 ± 5.63	-2.97
$A_1(TO_2)$	*	*	*	4.46	7.49 ± 1.08	*	5.98 ± 4.73	4.44
$A_1(TO_3)$	*	*	*	4.13	4.54 ± 1.24	*	-0.19 ± 1.4	0.65
$A_1(TO_4)$	*	*	*	5.70	-4.94 ± 0.65	*	-6.94 ± 0.60	-4.91
$E(TO_1)$	6.27 ± 0.63	5.97 ± 0.63	4.41 ± 0.60	$4.05/1.48$	*	0.40 ± 0.44	-0.15 ± 0.54	-0.61
$E(TO_2)$	5.48 ± 0.35	4.84 ± 0.35	1.56 ± 0.34	$-1.30/2.55$	*	0.61 ± 0.53	1.08 ± 1.51	-2.55
$E(TO_3)$	7.56 ± 1.04	5.81 ± 1.04	4.68 ± 1.07	$1.50/3.93$	*	1.46 ± 1.75	1.44 ± 7.44	0.50
$E(TO_4)$	4.5 ± 0.69	4.44 ± 0.69	2.42 ± 0.68	$0.22/3.80$	*	5.43 ± 0.92	-3.84 ± 11.74	2.40
$E(TO_5)$	*	*	*	$8.79/6.30$	*	*	*	-0.68
$E(TO_6)$	12.9 ± 1.85	11.13 ± 1.85	9.16 ± 2.02	$11.51/10.08$	*	0.72 ± 2.31	1.90 ± 1.9	-0.94
$E(TO_7)$	3.41 ± 0.68	1.64 ± 0.68	1.23 ± 0.82	$4.37/1.98$	*	7.21 ± 2.64	7.69 ± 0.59	4.75
$E(TO_8)$	8.56 ± 0.48	6.72 ± 0.48	3.27 ± 0.70	$-0.61/4.83$	*	6.73 ± 0.62	6.20 ± 5.94	3.35
$E(TO_9)$				$7.18/-0.67$			-7.95 ± 13.41	0.90
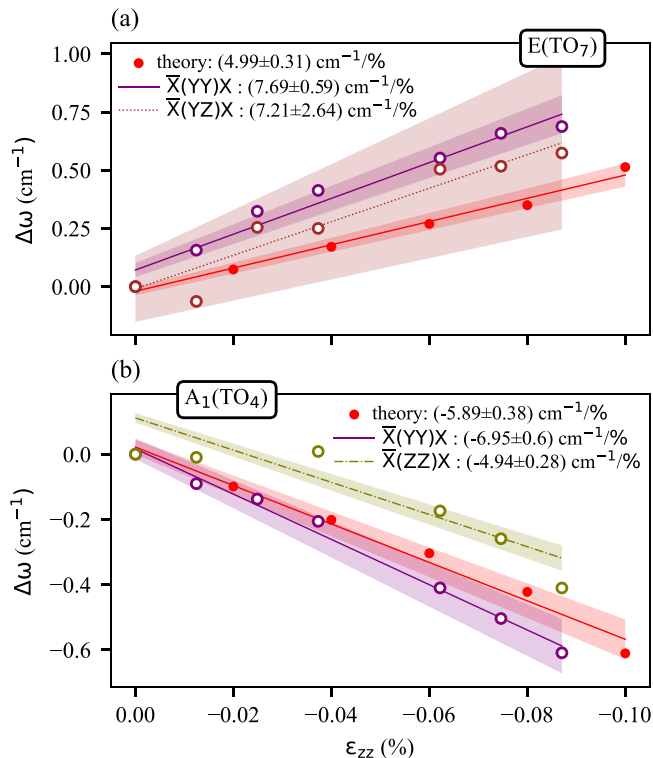
FIG. 7. Comparison of the theoretical stoichiometric and experimental 5 Mg-LN-z sample when compressing along the z direction for frequency shifts of (a) $E(TO_7)$ and (b) $A_1(TO_4)$. $E(TO_7)$ shows a positive slope whereas $A_1(TO_4)$ shows a negative slope for z compression.

confirms the prediction that the $E(TO_6)$ mode is the mode with the highest slope for x and y compressions. In comparison with Secs. III A and III B, the slopes for x compression are very similar to those for y compression.

As concluded from the experimental results in Sec. III A, the 5% MgO-doped LN responds equally well as the stoichiometric LN upon compression. We compare the 5 Mg-LN-z sample with theoretical data of stoichiometric LN for z compression. As theoretically predicted and confirmed by the experiment both $E(TO_7)$ and $A_1(TO_4)$ modes show a linear dependence on z compression [see Figs. 7(a) and 7(b)]. For the $E(TO_7)$ mode, no degeneracy lifting occurs for z compression, which can also be seen in the experimental data. This investigation provides another rule for characterizing compressed LN.

As described in Sec. III B the frequencies of most modes are linearly increasing with increasing compression. For a few modes, this is not the case, e.g., for the $A_1(TO_4)$ modes. For this mode, a linear decrease in frequency with increasing compression is theoretically predicted. This is consistent with experimental measurements as shown in Fig. 7(b). This unusual behavior can also be explained with the help of the eigenvectors. In Fig. 5, it can be seen that the oxygen ions move towards the positively charged niobium ions and then away from them. If z compression reduces the distance between the cations, then as the oxygen ions displace away from niobium, the restoring force towards niobium may be weakened by the shortened distance to the lithium ions, which

also exerts the Coulomb force on the negatively charged oxygen ions. Thus, the frequency for z compression might be reduced. In a similar way, this explanation can also be applied to $A_1(TO_1)$ modes. All other modes for comparison for z compression are shown in Table IV.

IV. CONCLUSIONS

Experimental and theoretical phonon frequencies as a function of uniaxial strain have been evaluated and compared for LN and LT. This investigation has shown that all phonon modes are affected by strain. Both theoretical and experimental results are consistent with the roughly linear behavior of the modes and can be reasonably explained by an analysis of the calculated eigenvectors. The linearity of the slopes confirms the previous works under hydrostatic pressure and under external electric fields [21,23].

Accordingly, the obtained slopes provide reference values for the peak shifts. Furthermore, with the help of the slopes, it is possible to characterize compressed LN crystals and, hence, the vicinity of domain walls and wave guides in LN. Our experimental and theoretical investigations show that x and y compressed LN has particularly high peak shifts for the $E(TO_{5/6})$ modes and z compressed LN for the $A_1(TO_2)$, $E(TO_7)$, and $E(TO_8)$ modes [23].

Furthermore, calculations have shown that the degeneracy of the E modes is lifted for x and y compressions upon symmetry reduction. The splitting has also been observed in our experiments when measured under different scattering geometries. Based on our theoretical and experimental investigations three rules can be formulated to characterize the direction of uniaxial compression of a LN sample using different scattering geometries. This only concerns the E modes. The sample is x compressed if higher-frequency shifts are observed for the $\overline{Z}(YY)Z$ geometry than for the $\overline{Z}(XY)Z$ and $\overline{Z}(XX)Z$ geometries when applying the same compressive stress. For y compression, the opposite is the case. In contrast, when no differences are observed between the frequency shift of the E modes for various scattering geometries, it can be concluded that the sample under investigation must be z compressed.

Furthermore, the calculation has shown that the behavior of LT under strain is not significantly different from that of LN. Experimentally, it has additionally revealed that the frequency shifts under compression of stoichiometric and 5% MgO-doped LN are comparable. As DWs in LN and LT can be represented in the first approximation as strained lattices, our investigation might be helpful to understand the Raman signal of DWs. Both LN and LT are optically nonlinear materials. Thus, it is expectable that the nonlinear optical properties, such as the frequency shift, have a dependence on the strain. Hence, further studies of strained samples, concerning e.g., their linear and nonlinear optical response might further help to characterize ferroelectric DWs. For this reason, the focus of our next investigations will be the optical response of these materials as a function of strain.

[1] G. D. Miller, R. G. Batchko, W. M. Tulloch, D. R. Weise, M. M. Fejer, and R. L. Byer, 42%-efficient single-pass cw second-harmonic generation in periodically poled lithium niobate, Opt. Lett. **22**, 1834 (1997).

[2] R. Mouras, M. D. Fontana, P. Bourson, and A. V. Postnikov, Lattice site of Mg ion in LiNbO$_3$ crystal determined by Raman spectroscopy, J. Phys.: Condens. Matter **12**, 5053 (2000).

[3] A. Yariv, S. S. Orlov, and G. A. Rakuljic, Holographic storage dynamics in lithium niobate: Theory and experiment, J. Opt. Soc. Am. B **13**, 2513 (1996).

[4] N. Iyi, K. Kitamura, F. Izumi, J. Yamamoto, T. Hayashi, H. Asano, and S. Kimura, Comparative study of defect structures in lithium niobate with different compositions, J. Solid State Chem. **101**, 340 (1992).

[5] A. Bartasyte, S. Margueron, T. Baron, S. Oliveri, and P. Boulet, Toward high-quality epitaxial LiNbO$_3$ and LiTaO$_3$ thin films for acoustic and optical applications, Adv. Mater. Interfaces **4**, 1600998 (2017).

[6] Y. Li, W. G. Schmidt, and S. Sanna, Defect complexes in congruent LiNbO$_3$ and their optical signatures, Phys. Rev. B **91**, 174106 (2015).

[7] Y. Furukawa, K. Kitamura, S. Takekawa, A. Miyamoto, M. Terao, and N. Suda, Photorefraction in LiNbO$_3$ as a function of [Li]/[Nb] and MgO concentrations, Appl. Phys. Lett. **77**, 2494 (2000).

[8] G. Stone and V. Dierolf, Influence of ferroelectric domain walls on the Raman scattering process in lithium tantalate and niobate, Opt. Lett. **37**, 1032 (2012).

[9] G. F. Nataf, M. Guennou, A. Haußmann, N. Barrett, and J. Kreisel, Evolution of defect signatures at ferroelectric domain walls in Mg-doped LiNbO$_3$, Phys. Status Solidi RRL **10**, 222 (2016).

[10] M. Rüsing, S. Neufeld, J. Brockmeier, C. Eigner, P. Mackwitz, K. Spychala, C. Silberhorn, W. G. Schmidt, G. Berth, A. Zrenner, and S. Sanna, Imaging of 180° ferroelectric domain walls in uniaxial ferroelectrics by confocal Raman spectroscopy: Unraveling the contrast mechanism, Phys. Rev. Mater. **2**, 103801 (2018).

[11] X. Wang, P. O. Weigel, J. Zhao, M. Ruesing, and S. Mookherjea, Achieving beyond-100-GHz large-signal modulation bandwidth in hybrid silicon photonics Mach Zehnder modulators using thin film lithium niobate, APL Photonics **4**, 096101 (2019).

[12] M. Rusing, P. O. Weigel, J. Zhao, and S. Mookherjea, Toward 3D integrated photonics including lithium niobate thin films: A bridge between electronics, radio frequency, and optical technology, IEEE Nanotechnol. Mag. **13**, 18 (2019).

[13] D. Zhu, L. Shao, M. Yu, R. Cheng, B. Desiatov, C. J. Xin, Y. Hu, J. Holzgrafe, S. Ghosh, A. Shams-Ansari, E. Puma, N. Sinclair, C. Reimer, M. Zhang, and M. Lončar, Integrated photonics on thin-film lithium niobate, Adv. Opt. Photonics **13**, 242 (2021).

[14] M. G. Vazimali and S. Fathpour, Applications of thin-film lithium niobate in nonlinear integrated photonics, Adv. Photonics **4**, 1 (2022).

[15] C. Wang, M. Zhang, B. Stern, M. Lipson, and M. Lončar, Nanophotonic lithium niobate electro-optic modulators, Opt. Express **26**, 1547 (2018).

[16] R. Takigawa, T. Tomimatsu, E. Higurashi, and T. Asano, Residual stress in lithium niobate film layer of LNOI/Si hybrid wafer fabricated using low-temperature bonding method, Micromachines **10**, 136 (2019).

[17] K. Prabhakar, R. J. Patton, and R. M. Reano, Stress reduction and wafer bow accommodation for the fabrication of thin film lithium niobate on oxidized silicon, J. Vac. Sci. Technol. B **39**, 062208 (2021).

[18] M. Friedrich, W. G. Schmidt, A. Schindlmayr, and S. Sanna, Optical properties of titanium-doped lithium niobate from time-dependent density-functional theory, Phys. Rev. Mater. **1**, 034401 (2017).

[19] G. Zisis, C. Y. J. Ying, P. Ganguly, C. L. Sones, E. Soergel, R. W. Eason, and S. Mailis, Enhanced electro-optic response in domain-engineered LiNbO$_3$ channel waveguides, Appl. Phys. Lett. **109**, 021101 (2016).

[20] S. Reitzig, M. Rüsing, J. Zhao, B. Kirbus, S. Mookherjea, and L. M. Eng, "Seeing is believing"—In-depth analysis by co-imaging of periodically-poled x-cut lithium niobate thin films, Crystals **11**, 288 (2021).

[21] G. Stone, B. Knorr, V. Gopalan, and V. Dierolf, Frequency shift of Raman modes due to an applied electric field and domain inversion in LiNbO$_3$, Phys. Rev. B **84**, 134303 (2011).

[22] M. D. Fontana and P. Bourson, Microstructure and defects probed by Raman spectroscopy in lithium niobate crystals and devices, Appl. Phys. Rev. **2**, 040602 (2015).

[23] J. Mendes-Filho, V. Lemos, and F. Cerdelra, Pressure dependence of the Raman spectra of LiNbO$_3$ and LiTaO$_3$, J. Raman Spectrosc. **15**, 367 (1984).

[24] A. M. Heyns and J. B. Clark, Effect of pressure on the Raman spectra of solids: 1-KC103, J. Raman Spectrosc. **14**, 342 (1983).

[25] T. Jach, S. Kim, V. Gopalan, S. Durbin, and D. Bright, Long-range strains and the effects of applied field at 180° ferroelectric domain walls in lithium niobate, Phys. Rev. B **69**, 064113 (2004).

[26] D. A. Scrymgeour, V. Gopalan, A. Itagi, A. Saxena, and P. J. Swart, Phenomenological theory of a single domain wall in

uniaxial trigonal ferroelectrics: Lithium niobate and lithium tantalate, Phys. Rev. B **71**, 184110 (2005).

[27] J. P. Perdew, J. A. Chevary, S. H. Vosko, K. A. Jackson, M. R. Pederson, D. J. Singh, and C. Fiolhais, Erratum: Atoms, molecules, solids, and surfaces: Applications of the generalized gradient approximation for exchange and correlation, Phys. Rev. B **48**, 4978(E) (1993).

[28] J. P. Perdew, K. Burke, and M. Ernzerhof, Generalized Gradient Approximation Made Simple, Phys. Rev. Lett. **77**, 3865 (1996).

[29] G. Kresse and J. Furthmüller, Efficient iterative schemes for ab initio total-energy calculations using a plane-wave basis set, Phys. Rev. B **54**, 11169 (1996).

[30] P. E. Blöchl, Projector augmented-wave method, Phys. Rev. B **50**, 17953 (1994).

[31] S. Sanna, S. Neufeld, M. Rüsing, G. Berth, A. Zrenner, and W. G. Schmidt, Raman scattering efficiency in LiTaO₃ and LiNbO₃ crystals, Phys. Rev. B **91**, 224302 (2015).

[32] A. W. Warner, M. Onoe, and G. A. Coquin, Determination of elastic and piezoelectric constants for crystals in class (3 m), J. Acoust. Soc. Am. **42**, 1223 (1967).

[33] The elastic compliance tensor is given in the Cartesian basis which is given by Weis *et al.* [55]. The applied rhombohedral unit cell is also oriented according to this standard orientation. However, the orientation is not yet unambiguously defined by this convention. In accordance with the standard orientation, the basis vector of the rhombohedral unit cell can point in either the Cartesian $+y$ or $-y$ direction. The former is the general case for the rhombohedral unit cell, and the latter is for the basis of the elastic compliance tensor. Hence, the basis of the elastic compliance tensor was rotated by $180°$ about the z axis by a basis transformation according to Ref. [56]. This basis transformation results in the same tensor elements, except from a sign change in $s_{14} \rightarrow -s_{14}$.

[34] W. G. Schmidt, F. Bechstedt, and G. P. Srivastava, III-V(110) surface dynamics from an ab initio frozen-phonon approach, Phys. Rev. B **52**, 2001 (1995).

[35] E. Singh, H. Beccard, Z. H. Amber, J. Ratzenberger, C. W. Hicks, M. Rüsing, and L. M. Eng, Tuning domain wall conductivity in bulk lithium niobate by uniaxial stress, Phys. Rev. B **106**, 144103 (2022).

[36] Henkel Loctite®, Loctite stycast 2850ft (2014).

[37] B. Kirbus, C. Godau, L. Wehmeier, H. Beccard, E. Beyreuther, A. Haußmann, and L. M. Eng, Real-time 3D imaging of nanoscale ferroelectric domain wall dynamics in lithium niobate single crystals under electric stimuli: Implications for domain-wall-based nanoelectronic devices, ACS Appl. Nano Mater. **2**, 5787 (2019).

[38] C. Godau, T. Kämpfe, A. Thiessen, L. M. Eng, and A. Haußmann, Enhancing the domain wall conductivity in lithium niobate single crystals, ACS Nano **11**, 4816 (2017).

[39] P. S. Bednyakov, B. I. Sturman, T. Sluka, A. K. Tagantsev, and P. V. Yudin, Physics and applications of charged domain walls, npj Comput. Mater. **4**, 65 (2018).

[40] C. S. Werner, S. J. Herr, K. Buse, B. Sturman, E. Soergel, C. Razzaghi, and I. Breunig, Large and accessible conductivity of charged domain walls in lithium niobate, Sci. Rep. **7**, 9862 (2017).

[41] A. Bartasyte, S. Margueron, A. M. Glazer, E. Simon, I. Gregora, S. Huband, and P. A. Thomas, Vibrational modes and over-

lap matrix of LiNb₁₋ₓTaₓO₃ mixed crystals, Phys. Rev. B **99**, 094306 (2019).

[42] M. Rüsing, S. Sanna, S. Neufeld, G. Berth, W. G. Schmidt, A. Zrenner, H. Yu, Y. Wang, and H. Zhang, Vibrational properties of LiNbO₁₋ₓTaₓO₃ mixed crystals, Phys. Rev. B **93**, 184305 (2016).

[43] S. Margueron, A. Bartasyte, A. M. Glazer, E. Simon, J. Hlinka, I. Gregora, and J. Gleize, Resolved E-symmetry zone-centre phonons in LiTaO₃ and LiNbO₃, J. Appl. Phys. **111**, 104105 (2012).

[44] A. Irzhak, D. Irzhak, V. Khvostikov, K. Pundikov, D. Roshchupkin, and R. Fahrtdinov, Effect of local changes in the composition of the LiNb₁₋ₓTaₓO₃ single crystal on the Raman spectra, J. Raman Spectrosc. **53**, 969 (2022).

[45] N. V. Sidorov and M. N. Palatnikov, Raman spectra of lithium niobate crystals heavily doped with zinc and magnesium, Opt. Spectrosc. **121**, 842 (2016).

[46] A. Ridah, P. Bourson, M. D. Fontana, and G. Malovichko, The composition dependence of the Raman spectrum and new assignment of the phonons in LiNbO₃, J. Phys.: Condens. Matter **9**, 9687 (1997).

[47] See Supplemental Material http://link.aps.org/supplemental/10.1103/PhysRevMaterials.7.024420 for a detailed description of our methods and an overview of all results.

[48] M. Tejerina, K. Pereira da Silva, A. Goñi, and G. Torchia, Hydrostatic-pressure dependence of raman-active optical phonons in Nd : Mg : LiNbo₃, Opt. Mater. (Amsterdam) **36**, 581 (2013).

[49] P. Hermet, M. Veithen, and P. Ghosez, First-principles calculations of the nonlinear optical susceptibilities and Raman scattering spectra of lithium niobate, J. Phys.: Condens. Matter **19**, 456202 (2007).

[50] D. Doratotaj, J. R. Simpson, and J.-A. Yan, Probing the uniaxial strains in MoS₂ using polarized Raman spectroscopy: A first-principles study, Phys. Rev. B **93**, 075401 (2016).

[51] M. Huang, H. Yan, C. Chen, D. Song, T. F. Heinz, and J. Hone, Phonon softening and crystallographic orientation of strained graphene studied by Raman spectroscopy, Proc. Natl. Acad. Sci. USA **106**, 7304 (2009).

[52] S. Pak, J. Lee, Y.-W. Lee, A.-R. Jang, S. Ahn, K. Y. Ma, Y. Cho, J. Hong, S. Lee, H. Y. Jeong, H. Im, H. S. Shin, S. M. Morris, S. Cha, J. I. Sohn, and J. M. Kim, Strain-mediated interlayer coupling effects on the excitonic behaviors in an epitaxially grown MoS₂/WS₂ van der Waals heterobilayer, Nano Lett. **17**, 5634 (2017).

[53] B. G. Oliveira, A. Zabardasti, H. Goudarziafshar, and M. Salehnassaj, The electronic mechanism ruling the dihydrogen bonds and halogen bonds in weakly bound systems of H₃SiH···HOX and H₃SiH···XOH (X = F, Cl, and Br), J. Mol. Model **21**, 77 (2015).

[54] R. E. Newnham, *Properties of Materials* (Oxford University Press, Oxford, 2004).

[55] R. S. Weis and T. K. Gaylord, Lithium niobate: Summary of physical properties and crystal structure, Appl. Phys. A: Solids Surf. **37**, 191 (1985).

[56] W. L. Bond, The mathematics of the physical properties of crystals, Bell Syst. Tech. J. **22**, 1 (1943).

[57] http://www.For5044.de.